2022-08-30

An event of extreme relativistic and ultra-relativistic electron enhancements following the arri...

Version	Published version
Citation (published version):	A. Nasi, C. Katsavrias, I. Daglis, I. Sandberg, S. Aminalragia-Giamini, W. Li, Y. Miyoshi, H. Evans, T. Mitani, A. Matsuoka, I. Shinohara, T. Takashima, T. Hori, G. Balasis. 2022. "An event of extreme relativistic and ultra-relativistic electron enhancements following the arrival of consecutive corotating interaction regions: Coordinated observations by Van Allen Probes, Arase, THEMIS and Galileo satellites" Front. Astron. Space Sci.. https://doi.org/10.3389/fspas.2022.949788

https://hdl.handle.net/2144/46483
Boston University

Check for updates

An event of extreme relativistic and ultra-relativistic electron enhancements following the arrival of consecutive corotating interaction regions: Coordinated observations by Van Allen Probes, Arase, THEMIS and Galileo satellites

Afroditi Nasi[1]*, Christos Katsavrias[1], Ioannis A. Daglis[1,2],
Ingmar Sandberg[3], Sigiava Aminalragia-Giamini[1,3], Wen Li[4],
Yoshizumi Miyoshi[5], Hugh Evans[6], Takefumi Mitani[7],
Ayako Matsuoka[8], Iku Shinohara[7], Takeshi Takashima[7],
Tomoaki Hori[5] and Georgios Balasis[9]

[1]Department of Physics, National and Kapodistrian University of Athens (NKUA), Athens, Greece,
[2]Hellenic Space Center (HSC), Athens, Greece, [3]Space Applications and Research Consultancy
(SPARC), Athens, Greece, [4]Center for Space Physics, Boston University, Boston, MA, United States,
[5]Institute for Space-Earth Environmental Research (ISEE), Nagoya University, Nagoya, Japan,
[6]European Space Research and Technology Centre (ESTEC), European Space Agency (ESA),
Noordwijk, Netherlands, [7]Institute of Space and Astronautical Science (ISAS), Japan Aerospace
Exploration Agency (JAXA), Tokyo, Japan, [8]Data Analysis Center for Geomagnetism and Space
Magnetism, Graduate School of Science, Kyoto University, Kyoto, Japan, [9]Institute for Astronomy,
Astrophysics, Space Applications and Remote Sensing (IAASARS), National Observatory of Athens
(NOA), Athens, Greece

During July to October of 2019, a sequence of isolated Corotating Interaction Regions (CIRs) impacted the magnetosphere, for four consecutive solar rotations, without any interposed Interplanetary Coronal Mass Ejections. Even though the series of CIRs resulted in relatively weak geomagnetic storms, the net effect of the outer radiation belt during each disturbance was different, depending on the electron energy. During the August-September CIR group, significant multi-MeV electron enhancements occurred, up to ultra-relativistic energies of 9.9 MeV in the heart of the outer Van Allen radiation belt. These characteristics deemed this time period a fine case for studying the different electron acceleration mechanisms. In order to do this, we exploited coordinated data from the Van Allen Probes, the Time History of Events and Macroscale Interactions during Substorms Mission (THEMIS), Arase and Galileo satellites, covering seed, relativistic and ultra-relativistic electron populations, investigating their Phase Space Density (PSD) profile dependence on the values of the second adiabatic invariant K, ranging from near-equatorial to off equatorial mirroring populations. Our results indicate that different acceleration mechanisms took place for

different electron energies. The PSD profiles were dependent not only on the μ value, but also on the K value, with higher K values corresponding to more pronounced local acceleration by chorus waves. The 9.9 MeV electrons were enhanced prior to the 7.7 MeV, indicating that different mechanisms took effect on different populations. Finally, all ultra-relativistic enhancements took place below geosynchronous orbit, emphasizing the need for more Medium Earth Orbit (MEO) missions.

1 Introduction

The outer Van Allen radiation belt is comprised by electron populations which undergo a complex mix of processes (Baker and Daglis, 2007; Reeves and Daglis, 2016; Daglis et al., 2019), overall leading to their energization, to their loss, or even to having no effect (Reeves et al., 2003; Turner et al., 2015a; Moya et al., 2017). For the acceleration process, the most important mechanisms are inward diffusion *via* drift-resonant interaction with Ultra-Low Frequency (ULF) Pc4-5 waves (Schulz and Lanzerotti, 1974; Shprits et al., 2008; Georgiou et al., 2015) and local acceleration *via* gyroresonant interaction with whistler mode chorus waves (Horne et al., 2005; Thorne et al., 2013; Jaynes et al., 2015; Bortnik et al., 2016). Nevertheless, wave-particle interactions with various wave modes can also lead to electron loss, through scattering into the atmosphere (Shprits et al., 2007; Jaynes et al., 2014; Usanova et al., 2014), while significant losses can occur due to direct or indirect magnetopause shadowing (Turner et al., 2012; Kim and Lee, 2014; Katsavrias et al., 2015a). This mechanism refers to electrons being lost to the interplanetary space by crossing the magnetosphere, with the two processes acting separately (Staples et al., 2022): in direct magnetopause shadowing, the compressing magnetopause crosses the electron drift paths, while, in indirect magnetopause shadowing, the electrons are transported outwards to the magnetopause by wave-particle interactions.

The response of the outer radiation belt electron populations can vary depending on the solar wind parameters, wave activity, and the source and seed electron populations abundance and intensity (Boyd et al., 2016; Katsavrias et al., 2019a; Nasi et al., 2020). Additionally, the response is dependent on the driver of the geomagnetic disturbance, e.g., Interplanetary Coronal Mass Ejections (ICMEs) or Stream Interaction Regions (SIRs) (Shen et al., 2017), even on the properties of the different parts of the drivers (e.g., sheath, ejecta) (Kilpua et al., 2015; Turner et al., 2019; Kalliokoski et al., 2022). Nevertheless, the High Speed Streams (HSSs) that follow an SIR have been shown to be particularly effective in producing multi-MeV electron enhancements, mainly because of intervals of combined southward Interplanetary Magnetic Field (IMF) and solar

wind velocity Vsw over 500 km/s, which lead to an enhanced magnetic reconnection rate at the dayside magnetopause (Borovsky and Denton, 2006; Miyoshi et al., 2013; Horne et al., 2018). In the case of persistent SIRs, when their sources corotate around the solar rotation axis so that the SIRs affect the magnetosphere more than once, the structures are usually called Corotating Interaction Regions (CIRs) instead of SIRs (Allen et al., 2020).

Also notable is the fact that the vast majority of the multi-MeV electron enhancement events are characterized by significant activity in both wave species, i.e., chorus and Pc4-5 ULF waves (Turner et al., 2013; Katsavrias et al., 2015b), which may be concurrent or exhibiting a time lag. Moreover, several simulations have indicated that both local acceleration by chorus and radial diffusion by ULF waves were needed to reproduce the observed relativistic electron flux (Li et al., 2016; Ma et al., 2016). One step further, Jaynes et al. (2015) proposed that for the acceleration of electrons at ultra-relativistic energies (higher than 2–3 MeV), a two-step acceleration is needed; first, a gyro-resonance acceleration of seed electrons to relativistic energies, and then further acceleration *via* inward radial diffusion by ULF Pc5 waves. This scenario was later verified by observations and simulation during the April-May 2017 event (Katsavrias et al., 2019b). Nevertheless, the latter authors indicated that this scenario was valid for electrons with energies up to 5 MeV, and it could not explain the energization of even more energetic electrons. On the other hand, Allison and Shprits, (2020) showed that extreme plasma density depletions may favor local heating of electrons up to 7.7 MeV due to rapid increase of the energy diffusion coefficients, thus suggesting an additional step to the acceleration. However, most studies which investigate the matter of the dominant acceleration mechanism, in contrast with loss mechanisms (Turner et al., 2014), are based on single values of the second adiabatic invariant (K), neglecting the impact of the two acceleration mechanisms on equatorial or off-equatorial mirroring electrons.

From a space weather point of view, this kind of events, leading to the energization of electrons up to or over 7.7 MeV, is quite rare, but poses a severe threat to space assets. Therefore, they are of great interest to the scientific community, and efforts

have been devoted to their prediction. In the scope of SafeSpace, a project funded by Horizon 2020 that aims at advancing space weather nowcasting and forecasting capabilities and, consequently, at contributing to the safety of space assets through the transition of powerful tools from research to operations, we examine the relative contribution of acceleration mechanisms during a group of Corotating Interaction Regions (CIRs) that impacted the magnetosphere for four consecutive solar rotations, leading to mostly moderate storms, that occurred during the second half of 2019 (Hajra and Sunny, 2022). However, only one out of the four CIR groups did result in extreme electron acceleration, leading to the enhancement of up to 9.9 MeV electrons in the heart of the outer radiation belt. This paper is the first part (observational part) of the study, where we exploit coordinated measurements from several spacecraft (Van Allen Probes, Galileo, Arase and THEMIS) to investigate the conditions that led to this multi-MeV electron enhancement, focusing on the evolution of Phase Space Density (PSD) radial profiles at different K values. The structure of the paper is as follows: in Section 2 we present the data and the methodology followed, in Section 3 we present a detailed description of the event, in terms of solar wind properties, geomagnetic parameters, wave activity, electron density and flux intensity, while in Section 4 we examine the electron PSD profiles.

2 Data selection and methodology

2.1 Solar wind parameters, geomagnetic indices, and wave activity

We obtain the 1-min resolution values of several solar wind parameters and geomagnetic indices from the NASA OMNIWeb database, i.e., the solar wind velocity (Vsw), the solar wind dynamic pressure (Psw), the z component of the Interplanetary Magnetic Field (IMF), and the geomagnetic index SYM-H. Using OMNIWeb data, we also calculate the location of the dayside magnetopause (L_{MP}), following the model of Shue et al. (1998), and the MLT-averaged location of the plasmapause (L_{PP}), following the model of O'Brien and Moldwin (2003). Additionally, we use 1-min resolution data of the SuperMAG Lower envelope (SML) auroral electrojet index from the SuperMAG database. The SML index (Gjerloev, 2012) is an extension of AL index, as it is calculated using data from up to 100 stations instead of 12, and is similarly used for the identification of substorms (Newell and Gjerloev, 2011).

For the Very Low Frequency (VLF) whistler-mode chorus waves, we use the Magnetic Local Time (MLT) averaged lower-band wave amplitude, corresponding to frequencies in the 0.1–0.5 f_{ce} range, where f_{ce} is the equatorial electron gyro-frequency (Li et al., 2013). The model uses precipitating electron fluxes measured by the Medium Energy Proton and

Electron Detector (MEPED) of the Space Environmental Monitor (SEM-2; Evans and Greer, 2004) on board the Polar Orbiting Environmental Satellites (POES) of the National Oceanic and Atmospheric Administration (NOAA) and the Meteorological Operational (Metop) satellites of the European Organization for the Exploitation of Meteorological Satellites (EUMETSAT). This method is derived from the electron precipitation driven by wave-particle interactions with chorus waves, and thus provides an extensive L and MLT coverage, as this constellation consists of up to six sun-synchronous satellites in Low Earth Orbit (LEO). The magnetic coordinates are provided by the POES and Metop ephemeris. Even though this method gives a proxy of VLF wave amplitude, it has the advantage of not being limited by the azimuthal location of the spacecraft. Therefore, we can have an estimation of the wave amplitude without needing multiple spacecraft in different MLTs, which is ideal for qualitative comparisons, such as the one in this study.

We note here that the method for the computation of the chorus wave amplitude does not produce L* values. Instead, we will cautiously use the provided L values, keeping in mind that the difference between L-L* values generally gradually increases with increasing radial distance. For a dipole-like magnetic field the L would be sufficient, but in the terrestrial magnetosphere the dipole approximation fades while moving outward. Additionally, this approximation is valid only during quiet times (Schulz and Lanzerotti, 1974), while, during active times, the modulations of the nightside magnetic field and dayside magnetopause should be accounted for, affecting the L-L* difference (Turner et al., 2014). However, for qualitative comparisons such as in this study, where we are mostly interested in the temporal dependence of the selected parameters, we believe that the use of both L and L* will not affect the nature of our results.

For the Ultra-Low Frequency (ULF) waves, we are interested in the Pc4-5 range (frequency of 2–25 mHz). We use their Power Spectral Density ($PSD_{B,E}$), acquired from the EU-H2020 SafeSpace database. The method of its computation is presented in Katsavrias et al. (2022), and uses magnetic and electric field measurements from the Flux Gate Magnetometer (FGM; Auster et al., 2008) and the Electric Fields Instrument (EFI; Bonnell et al., 2008) on board the Time History of Events and Macroscale Interactions during Substorms (THEMIS) A, D, and E satellites. For the magnetic coordinates, the International Radiation Belt Environment Modeling (IRBEM) library (Bourdarie and O'Brien, 2009) the Tsyganenko and Sitnov 2005 model (TS04; Tsyganenko and Sitnov, 2005) have been used.

2.2 Electron data

2.2.1 Electron density

For the electron density, we use (level-4) data from the Waves instrument of the Electric and Magnetic Field Instrument Suite

and Integrated Science (EMFISIS; Kletzing et al., 2013) instrument suite on board the Van Allen Probes (former Radiation Belt Storm Probes—RBSP), following Kurth et al. (2015). The magnetic coordinates are provided by the Energetic Particle, Composition, and Thermal Plasma instrument suite (ECT; Spence et al., 2013), calculated *via* the TS04 model. During the period of interest, only Van Allen Probe A was active (Probe B was terminated on 16/7/2019), so we use only the corresponding measurements hereafter.

2.2.2 Electron flux intensity

For the electron flux intensity in low L range ($L^* < 5.8$), we use data from the Van Allen Probe A and the Arase (or Exploration of energization and Radiation in Geospace—ERG) satellite (Miyoshi et al., 2018a), as the concurrent operation of the two missions in 2017–2019 provided a unique opportunity to obtain uniform-quality measurements used in several other studies (Miyoshi et al., 2022).

From the Van Allen Probe A, we use spin-averaged differential flux measurements (level-2 data) and pitch angle resolved differential flux measurements (level-3 data) from the Magnetic Electron Ion Spectrometer (MagEIS; Blake et al., 2013) and the Relativistic Electron Proton Telescope (REPT; Baker et al., 2012), where the magnetic coordinates are provided by the ECT suite with the use of the TS04 model. The MagEIS measurements are background corrected (Claudepierre et al., 2015), keeping data with less than 75% background error. The MagEIS and REPT measurements have been cross-calibrated (Sandberg et al., 2021) using measurements of the extremely high-energy electron experiment (XEP) instrument (Higashio et al., 2018) of the Arase satellite as a reference.

From the Arase satellite, we use unidirectional flux measurements (level-3) from the High-energy Electron Experiments (HEP; Mitani et al., 2018) instrument, both from its Low unit (HEP-L) and High unit (HEP-H), with the magnetic coordinates of the Arase ephemeris, calculated using the IRBEM library and the TS04 model. In this study, the measurements of HEP have been slightly rescaled using measurements from the XEP instrument as a reference, using the factors shown in Supplementary Tables S1, S2.

For the electron flux intensity in high L range ($L^* > 5.8$), we use data from the Galileo and THEMIS satellites.

From the Galileo spacecraft, we use omni-directional measurements (level-1, version 2; Sandberg et al., 2022) as derived by measurements from the Environment Monitoring Unit (EMU; Sandberg et al., 2019). The magnetic coordinates were derived using the UNILIB library (Heynderickx et al., 2000), assuming the International Geomagnetic Reference Field (IGRF) model for the internal, and the quiet Olson and Pfitzer, 1977 model (Olson and Pfitzer, 1977) for the external magnetic field components.

From the THEMIS A, D, and E spacecraft, we use pitch angle resolved data from the Solid State Telescope (SST; Angelopoulos

et al., 2008). The measurements have been processed and provided by ONERA-DPHY-ERS team. For the magnetic coordinates, the IRBEM library and the TS04 model have been used.

2.2.3 Electron phase space density

Using the aforementioned pitch angle resolved data, we calculate the electron Phase Space Density (PSD) as a function of the three adiabatic invariants (μ, K, and L^*), following Chen et al. (2005) and Nasi et al. (2020). As we want to keep track of specific electron populations, we define the following value ranges for the adiabatic invariants:

- μ = 100, 1,000, and 5,000 MeV/G, corresponding to seed, relativistic and ultra-relativistic electrons (E = 0.2–0.5 MeV, E = 1–2 MeV, E = 2.8–5 MeV respectively, at L^* = 4.5, for the selected K values).
- K = 0.03, 0.09, and 0.15 $G^{1/2}R_E$.
- L^* = 3–8 R_E, with dL^* = 0.1 R_E, to study the inner magnetosphere in detail.

To calculate the electron PSD, we use data from three distinct missions, in order to achieve an extensive coverage in MLT and L^*. In low L^* range, we use the electron flux data from MagEIS and REPT instruments of the Van Allen Probe A mentioned above, with the magnetic field (level-3) data of the FXG magnetometer (Kletzing et al., 2013). These are combined with the HEP-L and HEP-H electron flux data mentioned above, with the spin-averaged magnetic field (level-2) data of the Magnetic Field Experiment (MGF; Matsuoka et al., 2018) of Arase. In high L^* range, we use the electron flux data from SST instruments of THEMIS satellites mentioned above, with the magnetic field (level-2) data of the Fluxgate Magnetometers (FGM) of each spacecraft.

3 Event description and properties

3.1 Solar wind parameters and geomagnetic indices

The event we examine covers the period of July to October of 2019. Figure 1 presents the solar wind velocity (Vsw), the solar wind dynamic pressure (Psw), the z component of the interplanetary magnetic field (Bz), the geomagnetic index SYM-H, the SML auroral electrojet index, the location of the dayside magnetopause (L_{MP}) and the MLT-averaged location of the plasmapause (L_{PP}) plotted over the logarithm of the electron density (n_e), for the time period of 1/7/2019 to 15/10/2019. During this period, and approximately every 28 days, a group of Corotating Interaction Regions (CIRs) impacted the magnetosphere, as seen in the solar wind velocity and pressure time profiles (Figures 1A,B), dividing the full time period in four CIR groups of similar velocity structure. In each CIR group, a CIR followed by a slower stream (Vsw$_{max}$ ≈ 400–600 km/s) arrives,
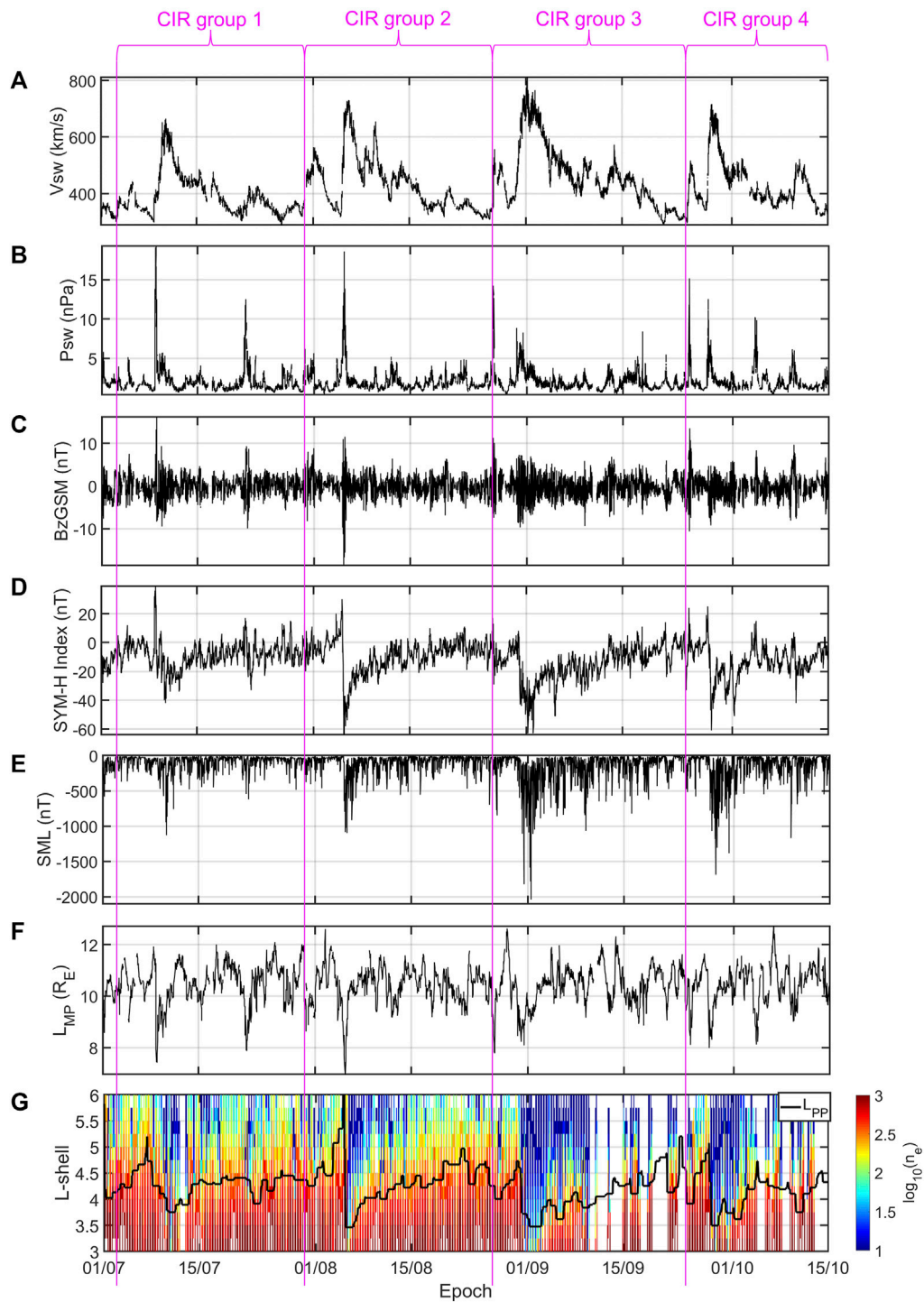
FIGURE 1
(A) The solar wind velocity Vsw (km/s), **(B)** the solar wind dynamic pressure Psw (nPa), **(C)** the southward component Bz (nT) of the interplanetary magnetic field, and **(D)** the geomagnetic index SYM-H (nT), all plotted using data form the OMNIWeb database. **(E)** The SML auroral electrojet index (nT; data from the SuperMAG database), **(F)** the location of the dayside magnetopause L_{MP} (R_E; calculated following the model of Shue et al. (1998), using data from the OMNIWeb database) and **(G)** the MLT-averaged location of the plasmapause L_{PP} (R_E; black line; calculated following the model of O'Brien & Moldwin (2003), using data from the OMNIWeb database) plotted over the logarithm of the electron density n_e (cm^{-3}; colored plot; calculated following Kurth et al. (2015), using data from the EMFISIS database; binned for dT = 3 h, dL = 0.25 R_E). All plots correspond to the time period of 1/7/2019 to 15/10/2019.

which is accompanied by a second CIR followed by the fastest stream of each group ($Vsw_{max} > 650$ km/s).

During the whole time period, we notice that the maximum velocity (Figure 1A) of the first stream of each group ranges between 440–570 km/s, and the maximum velocity of the fastest stream of each group ranges between 660–810 km/s. These maximums exhibit an increase, moving from the first to the third CIR group, with the fastest of all being the stream of the third CIR group, impacting the magnetosphere on 30/8 (12:00), which is also the most prolonged, with the Vsw remaining elevated for at least 10 days. Each fast stream coincides with a pressure pulse (Figure 1B), with a maximum ranging between 8–20 nPa. Even though the third group exhibits the largest maximum velocity, the pressure pulse it coincides with, arriving on 30/8, is the weakest in magnitude. The dynamic pressure reaches a maximum of only 8.8 nPa, but remains elevated (over 4 nPa) for at least 24 h.

Similarly, the behavior of the Bz component of the IMF (Figure 1C) during the third CIR group exhibits intense and prolonged fluctuations but with a rather small amplitude, only reaching up to ±10 nT, compared with the rest of the CIR groups that reach ±15 nT. Nevertheless, all groups, except for the first, result in the manifestation of moderate geomagnetic storms, reaching SYM-H $\approx$ −60 nT (Figure 1D), with the storm of the third group being again more prolonged than the rest, starting on 31/8 and returning to the pre-CIR levels after 12 days (11/9). Its SYM-H minimum value is −63 nT, reaching it twice, on 1/9 and 2/9. The combination of elevated solar wind velocity and persistently southward Bz results in an enhanced magnetic reconnection rate at the dayside magnetopause, which in turn leads to the main difference of the third group considering the geomagnetic impact; an extreme substorm. This is evident in the SML index (Figure 1E), which, after the fastest stream of the third group, reaches the values of −1800 nT on 31/8 and −2038 nT on 1/9, and even fluctuates at around or less than −1,000 nT for 3 days (from 31/8 to 2/9), while the rest of the CIR groups result in weaker and shorter substorm activity.

Following the behavior of the solar wind pressure, the magnetopause (Figure 1F) exhibits a big compression during the first and second CIR group, reaching between L = 7–8, but during the third and fourth groups the compression is moderate, hardly reaching L = 8. However, the magnetopause compression during the third group is again the most prolonged (1–3/9) as a result of the aforementioned enhanced reconnection rate at the dayside magnetopause. The location of the plasmapause (Figure 1G, black line) follows the behavior of the electron density very well in all CIR groups, except for the third, where it seems to reach a plateau at L = 3.5, indicating that the semi-empirical model of O'Brien and Moldwin (2003) does not adequately depict the plasmaspheric erosion during events such intense as the one of the third CIR group, even though it matches almost perfectly with the density patterns during the rest of the CIR groups. Additionally, the electron density (Figure 1G,

colored plot) seems to exhibit depletions after the fastest streams of each group, with the depletion following the third group being the most intense, reaching values under 10^2 cm^{-3} down to L = 3, remaining depleted for at least 3 days, and also remaining under $10^{2.5}$ cm^{-3} down to L = 4.5 for nearly 10 days.
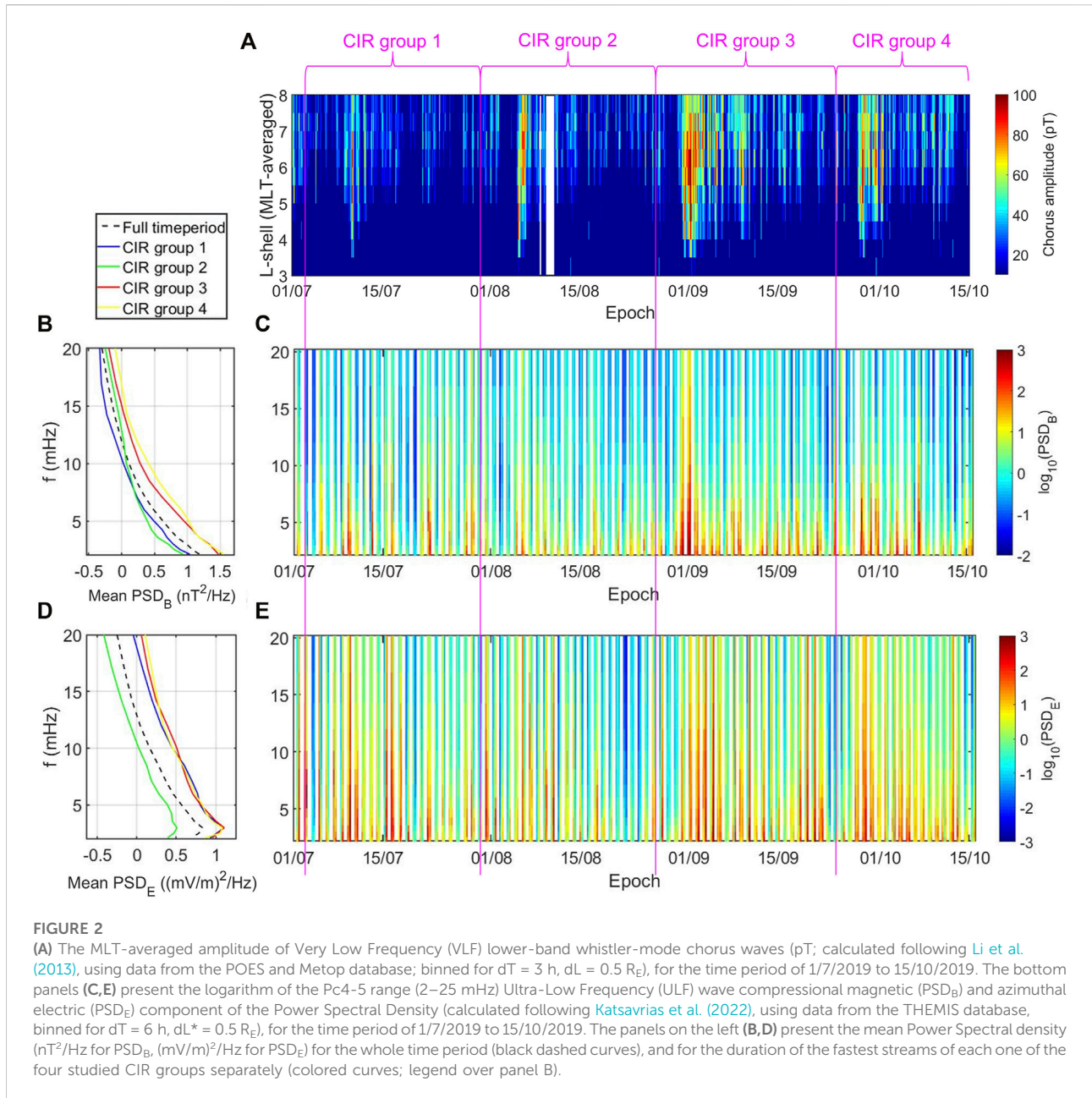
We notice that the substorm activity, the magnetopause compression, as well as the density depletions of the third and fourth CIR group exhibit similarities, even though the rest of the parameters are not so similar.

3.2 Wave activity

Considering the wave activity, Figure 2 presents the MLT-averaged whistler-mode chorus wave amplitude, and the logarithm of the compressional magnetic (PSD_B) and azimuthal electric (PSD_E) component of the Power Spectral Density of Ultra-Low Frequency (ULF) waves of the Pc4-5 range (2–25 mHz), along with the mean Power Spectral Density for the whole event duration, and for the duration of the fastest streams of the four studied CIR groups, separately.

We notice that the fastest CIR of each group results in chorus wave excitation (Figure 2A), generally in the range of L = 4–7.5. The third group exhibits the most intricate behavior, with the amplitude reaching approximately 80 pT on 31/8 (L = 4–7) and over 100 pT on 1/9, at the same L range, following the behavior of the SML index. By late 2/9 the activity moves outward (L > 6). The wave activity remains elevated during the course of the 10 days after the initial wave excitement. Overall, the third CIR group results in the most intense and prolonged chorus wave activity, following the extreme substorm activity. We note that the fourth CIR group exhibits also prolonged chorus activity, similar to the third group, that coincides with a significant and prolonged depletion of the electron density. Nevertheless, during the fourth CIR group, the chorus amplitudes are less intense, probably due the less intense substorm activity (in terms of SML index).

Considering the ULF Pc4-5 waves, we notice that both components of their Power Spectral Density (Figures 2C, E) exhibit the most prominent and persistent enhancements during the third CIR group, similar to the chorus activity. In detail, the compressional magnetic component PSD_B exhibits broadband oscillations, with power reaching over 10^2 nT^2/Hz during 30/8–2/9, with maximum that coincides with the maximum Psw. Similarly, the azimuthal electric component PSD_E reaches over 10^2 (mV/m)^2/Hz during 31/8–4/9, which coincides with Vsw >600 km/s. We note that the PSD_B of the third and fourth CIR groups are similar in mean power and more intense than the mean PSD_B of the first two groups. On the other hand, the mean PSD_E is similar during all groups except for the second, while all of the different time periods exhibit a peak wave activity at f $\approx$ 3 mHz, which corresponds to the drift frequencies of 1–2 MeV electrons.

FIGURE 2
(A) The MLT-averaged amplitude of Very Low Frequency (VLF) lower-band whistler-mode chorus waves (pT; calculated following Li et al. (2013), using data from the POES and Metop database; binned for dT = 3 h, dL = 0.5 R_E), for the time period of 1/7/2019 to 15/10/2019. The bottom panels **(C,E)** present the logarithm of the Pc4-5 range (2−25 mHz) Ultra-Low Frequency (ULF) wave compressional magnetic (PSD_B) and azimuthal electric (PSD_E) component of the Power Spectral Density (calculated following Katsavrias et al. (2022), using data from the THEMIS database, binned for dT = 6 h, dL* = 0.5 R_E), for the time period of 1/7/2019 to 15/10/2019. The panels on the left **(B,D)** present the mean Power Spectral density (nT^2/Hz for PSD_B, $(mV/m)^2$/Hz for PSD_E) for the whole time period (black dashed curves), and for the duration of the fastest streams of each one of the four studied CIR groups separately (colored curves; legend over panel B).

3.3 Electron flux intensity

Considering the response of the outer belt electrons during the four studied CIR groups, we examine the omni-directional electron fluxes during the studied period. Figure 3 presents the logarithm of the omni-directional electron flux intensity, using data from Van Allen Probe A and Galileo spacecraft, combining selected channels of similar energies for a full coverage of the inner magnetosphere, presenting seed (≈0.3 MeV), relativistic (≈1.8 MeV), and ultra-relativistic electrons (≈4.2, ≈7.7 and ≈9.9 MeV). Where available, the top panels (L = 5.5–8.5)

depict omni-directional flux (FEDO) from Galileo spacecraft, and the bottom panels (L = 2.5–5.5) depict spin-averaged differential flux (FESA) from Van Allen Probe A, with the selected energy channels mentioned on the right. (A more detailed version of Figure 3, focused only on the duration of the third CIR group, can be found in Supplementary Figure S1).

The seed electron fluxes (≈0.3 MeV, Figures 3A, B) exhibit significant enhancements following the substorm activity, as indicated by the SML index. The most intense and prolonged flux enhancement emerges after the fastest stream of the third group arrives, reaching fluxes over 10^7 (MeV cm² sr s)$^{-1}$ after 31/8

FIGURE 3
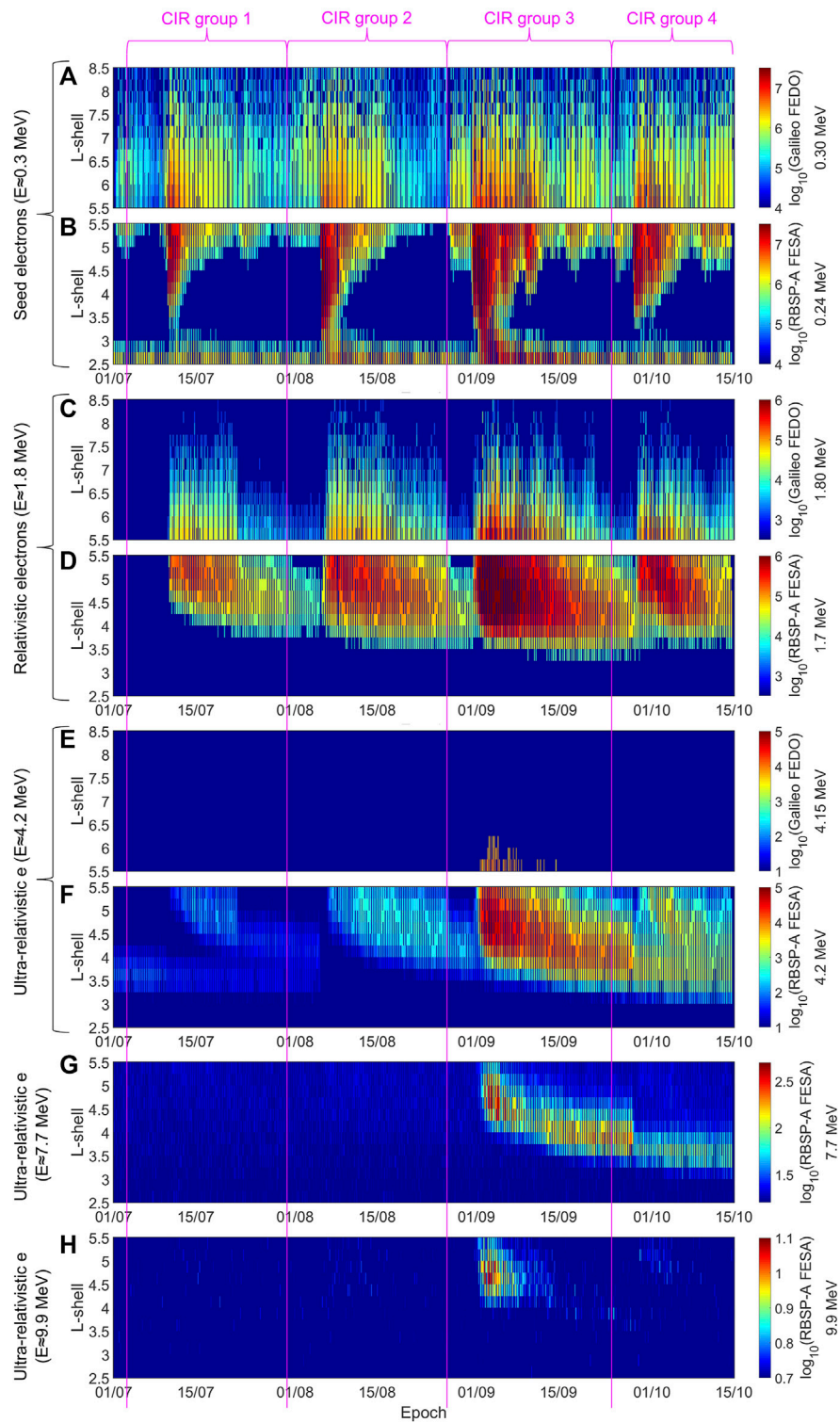The logarithm of electron flux intensity [(MeV cm² sr s)⁻¹] for seed [E ≈ 0.3 MeV, panels **(A,B)**], relativistic [E ≈ 1.8 MeV **(C,D)**] and ultra-relativistic electrons [E ≈ 4.2 MeV **(E,F)**, E ≈ 7.7 MeV **(G)**, E ≈ 9.9 MeV **(H)**] using data from Van Allen Probe A for L = 2.5−5.5 R$_E$ and from Galileo spacecraft for L = 5.5−8.5 R$_E$, binned for dT = 3 h, dL = 0.25 R$_E$, for the time period of 1/7/2019 to 15/10/2019. The selected energy channels of each spacecraft are mentioned on the right.

(06:00), with the maximum flux reaching over $10^{7.5}$ (MeV cm^2 sr s)$^{-1}$ emerging in L = 3.5–5.5 on 31/8 (12:00), 1/9 and 2/9. Over L = 3.5 the seed electron population slowly decays, with two more series of injections occurring in the next 10 days, with the outer radiation belt exhibiting fluxes of over $10^{6.5}$ (MeV cm^2 sr s)$^{-1}$ at L = 4–5.5. Under L = 3.5, after 1/9, the slot region gets filled with these seed electrons, remaining there for over 15 days.

Important features of the seed electron behavior are the following: Multiple injections, following the substorm activity, can be seen throughout the duration of the third CIR group, while the rest of the groups exhibit only one major injection with the seed electron fluxes gradually returning to their pre-event values. This multi-step filling of the outer radiation belt seems to characterize only the third group. This behavior leaves the outer belt to its initial state, following the first and second CIR groups, indicating that there is no significant pre-conditioning that could affect the efficiency of the third group in producing relativistic electrons. Additionally, the third group produces the most intense and persistent filling of the slot region, compared to the rest.

The relativistic electrons (≈1.8 MeV, Figures 3C, D) similarly exhibit a significant enhancement, after the fastest stream of the third group, which is the most prominent flux enhancement between the four groups. The fluxes reach over 10^5 (MeV cm^2 sr s)$^{-1}$ at L = 4.5–5.5 on 31/8 (15:00, namely 9 h after the seed electron enhancement), until 16/9. The strong enhancement reaches the lowest L values compared to the rest of the groups, down to L = 4. Generally, the fluxes remain intense until 27/9, when the next CIR arrives.

The ultra-relativistic electrons of ≈4.2 MeV (Figures 3E, F) are almost strictly measured by the Van Allen Probe A, as the Galileo satellite detected an enhancement only for some days during CIR group 3, and only under 6.6 R$_E$, which indicates that these electrons are confined inside of the geosynchronous orbit. In detail, the ≈4.2 MeV RBSP-A fluxes reach values over 10^4 (MeV cm^2 sr s)$^{-1}$ after 1/9 (09:00, namely 18 h after the ≈1.8 MeV electron enhancement). Furthermore, the ≈4.2 MeV population is progressively observed at lower L-shells (roughly down to L = 3.5).

Moving on, the ≈7.7 MeV electrons (which are only presented with data from the Van Allen Probes A REPT instrument; (Figure 3G) reach flux values over $10^{2.5}$ (MeV cm^2 sr s)$^{-1}$ on 2/9 (06:00, namely 21 h after the ≈4.2 MeV electron enhancement) at L = 4.5–5. The population moves inward, down to L = 3.75 up to 12/9, and then remains in the L = 3.75–4.25 range until 27/9. On the other hand, the ≈9.9 MeV electrons (Figure 3H) reach values over 10^1 (MeV cm^2 sr s)$^{-1}$ after 1/9 (21:00, namely 9 h before the ≈7.7 MeV electron enhancement; this is more evident in Supplementary Figure S1). The population rapidly decays remaining contained mostly at L = 4.5-5, until just 7/9. The third CIR group is the only one out of the whole studied period that leads to the enhancement of this population of electrons, up to almost

10 MeV, for at least half an order of magnitude, in the heart of the outer Van Allen radiation belt. The enhancement of the 9.9 MeV electrons before the 7.7 MeV population is peculiar. Nevertheless, we will not focus on this feature, as there are no PSD calculations available for these energies, thus, we cannot reach any robust conclusions on the mechanism or timing of their acceleration.

We note that, before the enhancements that follow the fastest streams of the CIR groups, the relativistic and ultra-relativistic electron populations lie at non-enhanced states, meaning that there is no pre-conditioning before the periods of the studied CIRs.

4 Electron phase space density results

Continuing our study, and in order to investigate the acceleration mechanisms leading to the aforementioned multi-MeV electron enhancements, we examine the Phase Space Density radial profiles focusing on the third CIR group. In Figure 4, the selected dates (28/8–3/9) cover the period from 2 days before the arrival of the CIR (28/8), until all the electron populations are enhanced, and the solar wind velocity begins to decrease. In detail, we present the radial profiles of the electron PSD, using data from Van Allen Probe A and Arase spacecraft for L*<5.8 (on the left of the vertical dashed lines) and from THEMIS spacecraft for L*>5.8 (on the right of the vertical dashed lines). As we have not performed any calibration to the THEMIS data, in order to produce smooth radial profiles, we have divided the THEMIS PSD by a factor of two for μ = 100 MeV/G and by a factor of six for μ = 1,000 MeV/G electrons; these values were selected based on the K = 0.03 G$^{1/2}$R$_E$ plots, in order to achieve a good alignment of the curves. Moreover, the electron PSD is presented for three selected values of the second adiabatic invariant: K = 0.03, 0.09, and 0.15 G$^{1/2}$R$_E$ (top, middle, bottom row panels of Figure 4, respectively). These K values correspond to populations ranging from near-equatorial to smaller equatorial pitch angles. Furthermore, the PSD is presented for three values of the first adiabatic invariant: μ = 100, 1,000, and 5,000 MeV/G (left, middle, right column panels of Figure 4, respectively). During the selected period, and at L* = 4.5, these μ values correspond to 0.2–0.5 MeV, 1–2 MeV, 2.8–5 MeV. This suggests that (at L* = 4.5) the value of μ = 100 MeV/G covers the seed electron population of ≈0.3 MeV (so we can compare with the fluxes of Figures 3A, B), the value of μ = 1,000 MeV/G covers the relativistic electron population of ≈1.8 MeV (fluxes of Figures 3C, D), but the value of μ = 5,000 MeV/G covers only the ultra-relativistic population of ≈4.2 MeV (fluxes of Figures 3E, F), and does not cover the ultra-relativistic populations of ≈7.7 and ≈9.9 MeV. In order to examine the PSD of these populations, we would need larger values of μ, which we do not have the coverage for,
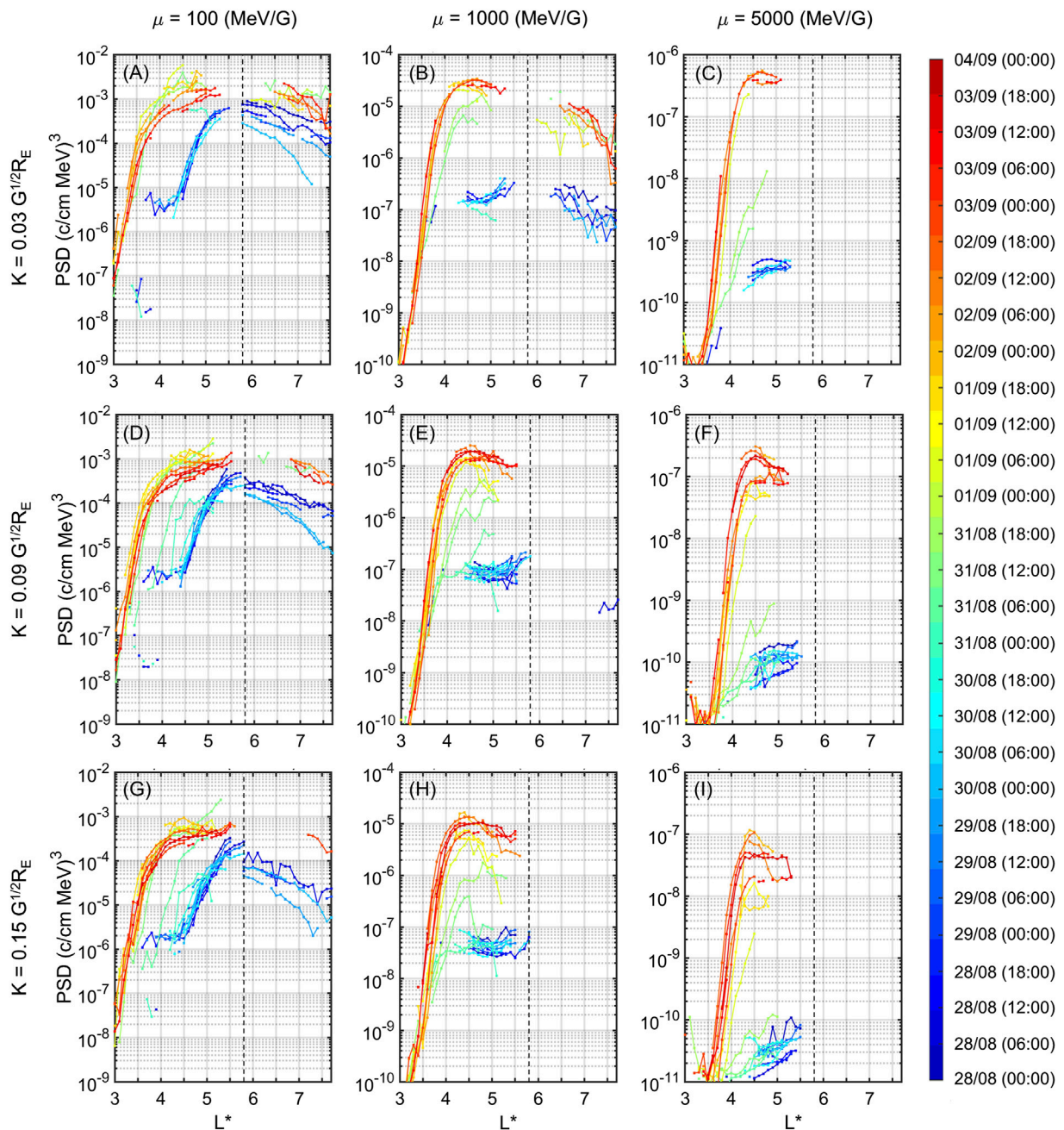
FIGURE 4
The radial profiles of the electron Phase Space Density (PSD), using data from the Van Allen Probe A and the Arase satellite for L* = 3−5.8 R$_E$ (on the left of the vertical dashed lines) and from the THEMIS A, D, and E satellites for L* = 5.8−7.8 R$_E$ (on the right of the vertical dashed lines) for selected dates of the third CIR group, during 28/8−4/9/2019. From top to bottom, the values of K = 0.03, 0.09, and 0.15 G$^{1/2}$R$_E$ are presented [panels **(A,B,C)**, **(D,E,F)**, and **(G,H,I)**, respectively]. From left to right, the values of μ = 100, 1,000, and 5,000 MeV/G are presented [panels **(A,D,G)**, **(B,E,H)**, and **(C,F,I)**, respectively]. The fastest CIR of the third CIR group arrives on 30/8, 12:00. The THEMIS PSD is presented here divided by a factor of two for μ = 100 MeV/G and divided by a factor of six for μ = 1,000 MeV/G. These values were selected based on the K = 0.03 G$^{1/2}$R$_E$ plots, in order to achieve a good alignment of the curves.

with these specific spacecraft. Moreover, we note that the aforementioned energy ranges per L* and per μ value are also affected by the values of K; so each of the 3 K values in

reality corresponds to even more strict energy ranges per population. (More information can be found at Supplementary Figure S2).

Considering the K = 0.03 $G^{1/2}R_E$ electrons, the μ = 100 MeV/G (Figure 4A) population exhibits significant enhancement at all L* values (approximately two orders of magnitude at L* = 4) that coincides with the beginning of the intense substorm activity (late 30/8, cyan to light green) and lasts until the end of the examined period. In agreement with the behavior of ≈1.8 MeV flux, the 1,000 MeV/G population (Figure 4B) increases on 31/8 (green) and exhibits clear rising peaks roughly at the L* = 4.5–5 range, indicating signatures of local acceleration by chorus waves. The latter is also in agreement with the significant intensification of chorus waves on 31/8 and at L = 4–7. Considering the 5,000 MeV/G population (Figure 4C), on the other hand, the behavior of the PSD is quite different, exhibiting a fast increase during 31/8 and 1/9 (from cyan to yellow) in the L* = 3.5-5 range, with the shape of the PSD, exhibiting increasing gradients, indicating radial diffusion driven by ULF waves. Nevertheless, we note that even though the latter scenario is possible (it would require a population of approximately 2 MeV beyond L* = 5, which is consistent with the observations in panel D of Figure 3), we cannot rule out the possibility of rising peaks beyond L* = 5 due to lack of available data (at such high energies only REPT on board RBSP-A provides flux measurements). After 4/9, both the 1,000 and 5,000 MeV/G populations exhibit gradual decrease at L*>4, which indicates outward radial diffusion and subsequent losses to the outer boundary. (This time period is shown in Supplementary Figure S3).

Continuing to the next value of K (0.09 $G^{1/2}R_E$, Figures 4D–F), we observe significant differences in the PSD radial profiles, especially for the ultra-relativistic population. The most striking difference, in comparison to the near equatorial population, is for the 5,000 MeV/G electrons (Figure 4F) that exhibit clear rising peaks, again at the L* = 4.5–5 range. At the same extent, the 1,000 MeV/G population (Figure 4E) exhibits an approximately two orders of magnitude enhancement, similar to the K = 0.03 $G^{1/2}R_E$, and rising peaks at the L* = 4.5-5 range, but the peaks are more pronounced compared to the lower K population. The aforementioned features of the relativistic and ultra-relativistic populations are even more pronounced as we move to higher K values (0.15 $G^{1/2}R_E$, Figure 4, panels H and I, respectively). After 4/9 (Supplementary Figure S3), the evolution of the PSD indicates gradual decrease at L*>4, similar to the K = 0.03 $G^{1/2}R_E$ population, for both the 1,000 and the 5,000 MeV/G electrons.

5 Discussion

During the second half of 2019, a sequence of Corotating Interaction Regions impacted the magnetosphere for four consecutive solar rotations, dividing the time period from July to October in four CIR groups of similar velocity structure. The high speed streams that follow such interaction regions are known to be more effective (compared to CMEs) in producing multi-MeV

electron enhancements (Miyoshi & Kataoka, 2005; Borovsky and Denton, 2006; Miyoshi et al., 2013; Horne et al., 2018) and this selected time period is particularly interesting, as it consists of a series of consecutive, well defined and isolated CIRs and HSSs without any interposed CMEs. Furthermore, we have shown that only one out of (more than) four CIRs was able to produce significant electron acceleration to ultra-relativistic energies. We must note that all four groups of CIRs exhibited similar minima and maxima of the SYM-H and Kp index, respectively, with SYM-H_{min} ≈ -60 nT and Kp_{max} ≈ 5.5. The fact that only one of the CIRs produced this multi-MeV electron enhancement emphasizes the discussion concerning the insufficiency of geomagnetic indices to characterize radiation belt dynamics (Schiller et al., 2014; Katsavrias et al., 2015a).

The solar wind parameters during these multi-MeV electron enhancements following the third CIR group were characterized by a combination of intense and prolonged Vsw and southward Bz, which led to enhanced rate of magnetic reconnection at the dayside magnetopause and, consequently, a series of intense substorm injections even down to L = 3. Even though all studied CIR groups resulted in moderate storms, they all led to seed electron injections at least down to L = 4. However, during the third CIR group, which was characterized by intense substorm activity (Turner et al., 2015), the injections were able to reach lower L-shells, even in the slot region. In turn, the intense substorm activity gave rise to intense chorus wave activity (Li et al., 2015; Rodger et al., 2022) for at least 10 days. Beside the intense chorus wave activity, there was also significant and broadband ULF wave activity in both the compressional magnetic and the azimuthal electric component, which in turn coincided with the prolonged pressure pulse of the corresponding interaction region and the high values of Vsw, respectively. This result is consistent with Katsavrias et al. (2022) who found a significant correlation between the magnetic and electric component of the radial diffusion coefficient and the solar wind pressure and speed, respectively. The concurrent activity of both wave species is a common feature during events with multi-MeV electron enhancements. As has been suggested by Simms et al. (2021), their combined effect is usually stronger than expected by the two wave species separately.

Considering the effect of this event on the omni-directional electron fluxes, we studied five main electron populations: seed electrons of ≈0.3 MeV, relativistic electrons of ≈1.8 MeV, and ultra-relativistic electrons of ≈4.2, ≈7.7 and ≈9.9 MeV. All populations exhibited no significant pre-conditioning. The combination of multiple seed electron injections to the inner magnetosphere and the relatively low dynamic pressure during the third CIR group led to minimal losses *via* magnetopause shadowing, thus sustaining the seed electron population in the outer belt. The most intriguing result was that, even though the flux increase exhibited a time-lag of a few hours for increasing energies up to 7.7 MeV, the 9.9 MeV electrons were enhanced approximately 9 h before the 7.7 MeV population. This suggests different acceleration mechanisms. Shprits et al. (2022) discussed

the fact that relativistic and ultra-relativistic electrons should be considered as completely different populations, since not only the latter are rarer, and occurring solely below geosynchronous orbit, but also due to the different acceleration and loss mechanisms involved. Our results are in agreement with this discussion and indicate an even more complicated behavior.

Concerning the long-lasting debate between radial diffusion and local acceleration, our observational results do not provide a robust conclusion. For the near-equatorial (K = 0.03 $G^{1/2}R_E$) core relativistic population (μ = 1,000 MeV/G, E = 1–2 MeV in the heart of the outer radiation belt), PSD radial profiles are consistent with the mechanism of gyro-resonant acceleration with chorus waves. On the other hand, for the near-equatorial (K = 0.03 $G^{1/2}R_E$) ultra-relativistic population (μ = 5,000 MeV/G, E = 2.8–5 MeV in the heart of the outer radiation belt), the increasing radial gradients in PSD suggest enhanced radial diffusion of approximately 2 MeV electrons from $L^\star$ = 5 to lower drift shells. Another supporting evidence for this two-step acceleration scenario is the 3 mHz peak in the ULF power spectral density. Nevertheless, our lack of sufficient high-energy electron flux measurements does not exclude the existence of rising peaks beyond $L^\star$ = 5 or simultaneous contribution from local acceleration driven by chorus waves. These results are also in agreement with Zhao et al. (2019) who conducted a superposed analysis using 19 storms with multi-MeV electron enhancements, verifying the two-step acceleration scenario, previously suggested by Jaynes et al. (2015). On the other hand, Katsavrias et al. (2019b) showed that in the case of the April-May event of 2017 the two-step acceleration scenario could not explain electron enhancements higher than 5 MeV, in the heart of the outer radiation belt, simply because it would require a population of approximately 6 MeV around geosynchronous orbit, which is not supported by REPT measurements. Recently, Allison et al. (2021) suggested that periods of significant depletion of electron density (less than 10 cm^{-3}) favor local acceleration up to 7.7 MeV due to abrupt increase of the energy diffusion coefficients. This feature exists also during the event studied in this paper. Nevertheless, it cannot explain the 9.9 MeV electron enhancement since the increase begins before the enhancement of 7.7 MeV electrons. Furthermore, the latter mechanism does not rule out the radial diffusion process concerning the μ = 5,000 MeV/G electrons (at least during this event), as the erosion of the plasmasphere down to low L-shells also favors the deep penetration of intense ULF waves (Georgiou et al., 2015). Unfortunately, the datasets used in this study do not allow the examination of PSD at such high energies. The aforementioned results indicate that the actual acceleration process possibly includes more than two steps.

Another important feature is the dependence of the PSD radial profile shape on the second adiabatic invariant. As shown by the results in (Figure 4 and Supplementary Figure S3), PSD at high K values exhibits more pronounced rising peaks concerning the core relativistic population. Moreover, chorus acceleration at high K values seems to be the dominant mechanism for the 5,000 MeV/G electron enhancement. This is consistent with the

fact that radial diffusion acts mostly on near-equatorial mirroring electrons (Elkington et al., 2003; Fei et al., 2006). The dependence of loss mechanisms on the second adiabatic invariant has been investigated in several studies (Turner et al., 2014; Usanova et al., 2014). Here we argue that a more comprehensive investigation of the dependence of acceleration mechanisms on K is required.

6 Conclusion

We studied the period of July to October 2019, when a sequence of consecutive, well defined, and isolated Corotating Interaction Regions impacted the magnetosphere for four consecutive solar rotations, dividing the time period in four CIR groups of similar velocity structure, without any interposed Interplanetary Coronal Mass Ejections. Even though the four CIR groups resulted in similar geomagnetic storm activity, only the third out of the four groups exhibited intense substorm activity and resulted in prolonged chorus and Pc4-5 wave activity, as well as significant multi-MeV electron enhancements up to 9.9 MeV in the heart of the outer Van Allen radiation belt.

In this, observation-based, part of our study, we exploited data from several missions (Van Allen Probes, Galileo, Arase, THEMIS) in order to investigate the properties of the third CIR group, covering August to mid-September of 2019. We presented PSD radial profiles for three electron populations (μ = 100, 1,000, and 5,000 MeV/G), investigating their PSD radial profile dependence on the values of the second adiabatic invariant K, ranging from near-equatorial to off equatorial mirroring populations. Our results concerning the third CIR group are summarized as follows:

- The combination of elevated Vsw along with persistently southward Bz resulted in enhanced magnetic reconnection at the dayside magnetopause, leading to the manifestation of an extreme substorm series, followed by intense seed electron injections to the inner magnetosphere, which in turn led to the excitation of chorus waves.
- The elevated Vsw and prolonged Psw pulse led to the excitation of ULF Pc4-5 waves, with the magnetic component of their power spectral density following the behavior of the Psw, and the electric component following the behavior of Vsw.
- Even though the flux increase exhibited few hours of time-lag between the seed, relativistic and ultra-relativistic electrons, the 9.9 MeV electrons were enhanced before the 7.7 MeV population, suggesting that different acceleration mechanisms take effect for each population.
- The depletion of electron density may have played a role in the observed electron acceleration *via* the increase of energy diffusion coefficients, but this mechanism seems

to be able to support the acceleration of electrons only up to 7.7 MeV.

- The combination of multiple seed electron injections, along with minimal losses *via* magnetopause shadowing, as a result of low Psw, sustained the seed electron population in the outer radiation belt, which seems to be an important condition of efficient acceleration.
- All ultra-relativistic electron populations were enhanced below geosynchronous orbit, indicating that MEO missions should be required for studying these populations effectively.
- The fact that only one out of the four studied CIR groups produced such an intense multi-MeV electron enhancement emphasizes that the common geomagnetic indices (e.g., SYM-H, Kp) are insufficient in characterizing radiation belt dynamics.
- The PSD profiles of near-equatorial mirroring electrons ($K = 0.03$ $G^{1/2}R_E$) indicated that local acceleration by chorus waves was dominant for the relativistic electrons ($\mu = 1,000$ MeV/G, E = 1–2 MeV at $L^* = 4.5$)
- Even though the lack of sufficient data made the determination of the dominant acceleration mechanism unclear, the 5,000 MeV/G population was probably enhanced *via* inward radial diffusion driven by Pc4-5 waves.
- The electron PSD profiles are dependent on the chosen values of the second adiabatic invariant, with higher K values corresponding to more pronounced local acceleration by chorus waves; however, this may be due to the radial diffusion being more effective on near-equatorial mirroring populations.

A comprehensive investigation of the dependence of acceleration mechanisms on K, combined with simulations of the outer belt at different μ values, is required in order to reach any robust conclusions.

Data availability statement

The following publicly available datasets were used in this study. The NASA OMNIWeb database can be found at: https:// omniweb.gsfc.nasa.gov/. The SuperMAG database is available at: https://supermag.jhuapl.edu/. Data from POES&Metop satellites are provided at: https://www.ngdc.noaa.gov/stp/ satellite/poes/dataaccess.html. The SafeSpace database can be accessed at: https://synergasia.uoa.gr/modules/document/? course=PHYS120. The THEMIS satellite measurements used for the creation of the EU-H2020 SafeSpace database can be found at: http://themis.ssl.berkeley.edu/data_products/index. php. The EMFISIS density database is provided at: https:// emfisis.physics.uiowa.edu/Flight/RBSP-A/L4/2019/. The Van Allen Probes data are available at: https://rbsp-ect.

newmexicoconsortium.org/data_pub/. The Arase (ERG) science data are provided by the ERG Science Center operated by ISAS/JAXA and ISEE/Nagoya University at: https://ergsc.isee.nagoya-u.ac.jp/index.shtml.en (Miyoshi et al., 2018b). The present study analyzed MGF-L2 8 s spin-averaged data v03_04 and v04_04 (10.34515/DATA.ERG-06001), HEP-L3 pitch angle sorted electron flux data v01_00 (10.34515/DATA.ERG-01002), and Orbit L3 v01 data (10. 34515/DATA.ERG-12001). Galileo data are available to users from European member states registered at the European Global Navigation Satellite Systems Agency (GNSS) science support centre website: https://gssc.esa.int/. The ONERA/ THEMIS flux database is available at: https://craterre.onera. fr/data/THEMIS_A/sste/cdf/.

Author contributions

AN has prepared the manuscript and analyzed the data. CK has contributed to the manuscript preparation, the data analysis, and has developed the software for calculating the electron PSD. ISa has provided access to the Galileo satellite data, and has provided the calibration factors for Galileo, Van Allen Probes and Arase electron fluxes. SA-G has contributed to the SafeSpace database. ID and GB have contributed to the interpretation of the results. WL has developed the method of inferring the chorus wave amplitude and has produced the corresponding chorus wave amplitude data. YM, HE, TM, AM, ISh, TT, and TH have contributed to the provision of data. All authors contributed to the article and approved the submitted version.

Conflict of interest

Authors ISa and SA-G are co-founders of Space Applications and Research Consultancy (SPARC).

The remaining authors declare that the research was conducted in the absence of any commercial or financial relationships that could be construed as a potential conflict of interest.

Publisher's note

All claims expressed in this article are solely those of the authors and do not necessarily represent those of their affiliated organizations, or those of the publisher, the editors and the reviewers. Any product that may be evaluated in this article, or claim that may be made by its manufacturer, is not guaranteed or endorsed by the publisher.

Supplementary material

The Supplementary Material for this article can be found online at: https://www.frontiersin.org/articles/10.3389/fspas.2022.949788/full#supplementary-material

References

Allen, R. C., Ho, G. C., Jian, L. K., Mason, G. M., Vines, S. K., and Lario, D. (2020). Predictive capabilities and limitations of stream interaction region observations at different solar longitudes. *Space weather.* 18, e2019SW002437. doi:10.1029/2019SW002437

Allison, H. J., and Shprits, Y. Y. (2020). Local heating of radiation belt electrons to ultra-relativistic energies. *Nat. Commun.* 11, 4533. doi:10.1038/s41467-020-18053-z

Allison, H. J., Shprits, Y. Y., Zhelavskaya, I. S., Wang, D., and Smirnov, A. G. (2021). Gyroresonant wave-particle interactions with chorus waves during extreme depletions of plasma density in the Van Allen radiation belts. *Sci. Adv.* 7 (5), eabc0380. doi:10.1126/sciadv.abc0380

Angelopoulos, V., Sibeck, D., Carlson, C. W., McFadden, J. P., Larson, D., Lin, R. P., et al. (2008). First results from the THEMIS mission. *Space Sci. Rev.* 141 (1-4), 453–476. doi:10.1007/s11214-008-9378-4

Auster, H. U., Glassmeier, K. H., Magnes, W., Aydogar, O., Baumjohann, W., Constantinescu, D., et al. (2008). The THEMIS fluxgate magnetometer. *Space Sci. Rev.* 141, 235–264. doi:10.1007/s11214-008-9365-9

Baker, D., and Daglis, I. A. (2007). "Radiation belts and ring current," in *Space weather - Physics and effects* (Berlin, Heidelberg: Springer Praxis Books, Springer), 173–202. doi:10.1007/978-3-540-34578-7_6

Baker, D. N., Kanekal, S. G., Hoxie, V. C., Batiste, S., Bolton, M., Li, X., et al. (2012). The relativistic electron–proton telescope (REPT) instrument on board the radiation belt storm Probes (RBSP) spacecraft: Characterization of earth's radiation belt high-energy particle populations. *Space Sci. Rev.* 65 (11), 337–381. doi:10.1007/s11214-012-9950-9

Blake, J. B., Carranza, P. A., Claudepierre, S. G., Clemmons, J. H., Crain, W. R., Dotan, Y., et al. (2013). The magnetic electron ion spectrometer (MagEIS) instruments aboard the radiation belt storm Probes (RBSP) spacecraft. *Space Sci. Rev.* 179, 383–421. doi:10.1007/s11214-013-9991-8

Bonnell, J. W., Mozer, F. S., Delory, G. T., Hull, A. J., Ergun, R. E., Cully, C. M., et al. (2008). The electric field instrument (EFI) for THEMIS. *Space Sci. Rev.* 141, 303–341. doi:10.1007/s11214-008-9469-2

Borovsky, J. E., and Denton, M. H. (2006). Differences between CME-driven storms and CIR-driven storms. *J. Geophys. Res.* 111, A07S08. doi:10.1029/2005JA011447

Bortnik, J., Thorne, R. M., Li, W., and Tao, X. (2016). "Chorus waves in geospace and their influence on radiation belt dynamics," in *Waves, particles, and storms in Geospace: A complex interplay*, 193–212. Editors G. Balasis, I. A. Daglis, and I. R. Mann (Oxford University Press). 9780198705246. doi:10.1093/acprof:oso/9780198705246.003.0009

Bourdarie, S., and O'Brien, T. P. (2009). International radiation belt environment modelling library. *Space Res. Today* 174, 27–28. doi:10.1016/j.srt.2009.03.006

Boyd, A. J., Spence, H. E., Huang, C.-L., Reeves, G. D., Baker, D. N., Turner, D. L., et al. (2016). Statistical properties of the radiation belt seed population. *J. Geophys. Res. Space Phys.* 121, 7636–7646. doi:10.1002/2016JA022652

Chen, Y., Friedel, R. H. W., Reeves, G. D., Onsager, T. G., and Thomsen, M. F. (2005). Multisatellite determination of the relativistic electron phase space density at geosynchronous orbit: Methodology and results during geomagnetically quiet times. *J. Geophys. Res.* 110, A10210. doi:10.1029/2004JA010895

Claudepierre, S. G., O'Brien, T. P., Blake, J. B., Fennell, J. F., Roeder, J. L., Clemmons, J. H., et al. (2015). A background correction algorithm for Van Allen Probes MagEIS electron flux measurements. *JGR. Space Phys.* 120 (7), 5703–5727. doi:10.1002/2015JA021171

Daglis, I. A., Katsavrias, C., and Georgiou, M. (2019). From solar sneezing to killer electrons: Outer radiation belt response to solar eruptions. *Phil. Trans. R. Soc. A* 377 (2148), 20180097. doi:10.1098/rsta.2018.0097

Elkington, S. R., Hudson, M. K., and Chan, A. A. (2003). Resonant acceleration and diffusion of outer zone electrons in anasymmetric geomagnetic field. *J. Geophys. Res.* 108 (A3), 1116. doi:10.1029/2001JA009202

Evans, D. S., and Greer, M. S. (2004). *Polar orbiting environmental satellite space environment monitor – 2: Instrument descriptions and archive data documentation (Technical Report No. version 1.4)*. Boulder, Colorado: Space Environment Center.

Fei, Y., Chan, A. A., Elkington, S. R., and Wiltberger, M. J. (2006). Radial diffusion and MHD particle simulations of relativistic electron transport by ULF waves in the September 1998 storm. *J. Geophys. Res.* 111, A12209. doi:10.1029/2005JA011211

Georgiou, M., Daglis, I. A., Zesta, E., Balasis, G., Mann, I. R., Katsavrias, C., et al. (2015). Association of radiation belt electron enhancements with earthward penetration of Pc5 ULF waves: A case study of intense 2001 magnetic storms. *Ann. Geophys.* 33, 1431–1442. doi:10.5194/angeo-33-1431-2015

Gjerloev, J. W. (2012). The SuperMAG data processing technique. *J. Geophys. Res.* 117, A09213. doi:10.1029/2012JA017683

Hajra, R., and Sunny, J. V. (2022). Corotating interaction regions during solar cycle 24: A study on characteristics and geoeffectiveness. *Sol. Phys.* 297, 30. doi:10.1007/s11207-022-01962-1

Heynderickx, D., Kruglanski, M., Quaghebeur, B., Speelman, E., and Daly, E. J. (2000). An overview and discussion of SPENVIS, ESA's space environment information System, and UNILIB, a fortran library of magnetic field utilities. SAE International. doi:10.4271/2000-01-2415

Higashio, N., Takashima, T., Shinohara, I., and Matsumoto, H. (2018). The extremely high-energy electron experiment (XEP) onboard the Arase (ERG) satellite. *Earth Planets Space* 70, 134. doi:10.1186/s40623-018-0901-x

Horne, R. B., Phillips, M. W., Glauert, S. A., Meredith, N. P., Hands, A. D. P., Ryden, K. A., et al. (2018). Realistic worst case for a severe space weather event driven by a fast solar wind stream. *Space weather.* 16, 1202–1215. doi:10.1029/2018SW001948

Horne, R. B., Thorne, R. M., Glauert, S. A., Albert, J. M., Meredith, N. P., and Anderson, R. R. (2005). Timescale for radiation belt electron acceleration by whistler mode chorus waves. *J. Geophys. Res.* 110, A03225. doi:10.1029/2004JA010811

Jaynes, A. N., Baker, D. N., Singer, H. J., Rodriguez, J. V., Loto'aniu, T. M., Ali, A. F., et al. (2015). Source and seed populations for relativistic electrons: Their roles in radiation belt changes. *JGR. Space Phys.* 120, 7240–7254. doi:10.1002/2015JA021234

Jaynes, A. N., Li, X., Schiller, Q. G., Blum, L. W., Tu, W., Turner, D. L., et al. (2014). Evolution of relativistic outer belt electrons during an extended quiescent period. *JGR. Space Phys.* 119, 9558–9566. doi:10.1002/2014JA020125

Kalliokoski, M. M. H., Kilpua, E. K. J., Osmane, A., Jaynes, A. N., Turner, D. L., George, H., et al. (2022). Phase space density analysis of outer radiation belt electron energization and loss during geoeffective and nongeoeffective sheath regions. *JGR. Space Phys.* 127, e2021JA029662. doi:10.1029/2021JA029662

Katsavrias, C., Daglis, I. A., Li, W., Dimitrakoudis, S., Georgiou, M., Turner, D. L., et al. (2015b). Combined effects of concurrent Pc5 and chorus waves on relativistic electron dynamics. *Ann. Geophys.* 33, 1173–1181. doi:10.5194/angeo-33-1173-2015

Katsavrias, C., Daglis, I. A., and Li, W. (2019a). On the statistics of acceleration and loss of relativistic electrons in the outer radiation belt: A superposed epoch analysis. *J. Geophys. Res. Space Phys.* 124, 2019JA026569–2768. doi:10.1029/2019JA026569

Katsavrias, C., Daglis, I. A., Turner, D. L., Sandberg, I., Papadimitriou, C., Georgiou, M., et al. (2015a). Nonstorm loss of relativistic electrons in the outer radiation belt. *Geophys. Res. Lett.* 42 (10), 521–530. doi:10.1002/2015GL066773

Katsavrias, C., Nasi, A., Daglis, I. A., Aminalragia-Giamini, S., Dahmen, N., Papadimitriou, C., et al. (2022). The "SafeSpace" database of ULF power spectral density and radial diffusion coefficients: Dependencies and application to simulations. *Ann. Geophys.* 40, 379–393. doi:10.5194/angeo-40-379-2022

Katsavrias, C., Sandberg, I., Li, W., Podladchikova, O., Daglis, I. A., Papadimitriou, C., et al. (2019b). Highly relativistic electron flux enhancement during the weak geomagnetic storm of April–May 2017. *J. Geophys. Res. Space Phys.* 124, 4402–4413. doi:10.1029/2019JA026743

Kilpua, E. K. J., Hietala, H., Turner, D. L., Koskinen, H. E. J., Pulkkinen, T. I., Rodriguez, J. V., et al. (2015). Unraveling the drivers of the storm time radiation belt response. *Geophys. Res. Lett.* 42, 3076–3084. doi:10.1002/2015GL063542

Kim, K.-C., and Lee, D.-Y. (2014). Magnetopause structure favorable for radiation belt electron loss. *J. Geophys. Res. Space Phys.* 119, 5495–5508. doi:10.1002/2014JA019880

Kletzing, C. A., Kurth, W. S., Acuna, M., MacDowall, R. J., Torbert, R. B., Averkamp, T., et al. (2013). The electric and magnetic field instrument suite and integrated science (EMFISIS) on RBSP. *Space Sci. Rev.* 179, 127–181. doi:10.1007/s11214-013-9993-6

Kurth, W. S., De Pascuale, S., Faden, J. B., Kletzing, C. A., Hospodarsky, G. B., Thaller, S., et al. (2015). Electron densities inferred from plasma wave spectra obtained by the Waves instrument on Van Allen Probes. *JGR. Space Phys.* 120, 904–914. doi:10.1002/2014JA020857

Li, W., Ma, Q., Thorne, R. M., Bortnik, J., Zhang, X.-J., Li, J., et al. (2016). Radiation belt electron acceleration during the 17 march 2015 geomagnetic storm: Observations and simulations. *JGR. Space Phys.* 121, 5520–5536. doi:10.1002/2016JA022400

Li, W., Ni, B., Thorne, R. M., Bortnik, J., Green, J. C., Kletzing, C. A., et al. (2013). Constructing the global distribution of chorus wave intensity using measurements of electrons by the POES satellites and waves by the Van Allen Probes. *Geophys. Res. Lett.* 40, 4526–4532. doi:10.1002/grl.50920

Li, W., Thorne, R. M., Bortnik, J., Baker, D. N., Reeves, G. D., Kanekal, S. G., et al. (2015). Solar wind conditions leading to efficient radiation belt electron acceleration: A superposed epoch analysis. *Geophys. Res. Lett.* 42, 6906–6915. doi:10.1002/2015GL065342

Ma, Q., Li, W., Thorne, R. M., Nishimura, Y., Zhang, X.-J., Reeves, G. D., et al. (2016). Simulation of energy-dependent electron diffusion processes in the Earths outer radiation belt. *JGR. Space Phys.* 121, 4217–4231. doi:10.1002/2016JA022507

Matsuoka, A., Teramoto, M., Nomura, R., Nose, M., Fujimoto, A., Tanaka, Y., et al. (2018). The ARASE (ERG) magnetic field investigation. *Earth Planets Space* 70, 43. doi:10.1186/s40623-018-0800-1

Mitani, T., Takashima, T., Kasahara, S., Miyake, W., and Hirahara, M. (2018). High-energy electron experiments (HEP) aboard the ERG (Arase) satellite. *Earth Planets Space* 70, 77. doi:10.1186/s40623-018-0853-1

Miyoshi, Y., Hori, T., Shoji, M., Teramoto, M., Chang, T. F., Segawa, T., et al. (2018b). The ERG science center. *Earth Planets Space* 70, 96. doi:10.1186/s40623-018-0867-8

Miyoshi, Y., Kataoka, R., Kasahara, Y., Kumamoto, A., Nagai, T., and Thomsen, M. F. (2013). High-speed solar wind with southward interplanetary magnetic field causes relativistic electron flux enhancement of the outer radiation belt via enhanced condition of whistler waves. *Geophys. Res. Lett.* 40 (17), 4520–4525. doi:10.1002/grl.50916

Miyoshi, Y., and Kataoka, R. (2005). Ring current ions and radiation belt electrons during geomagnetic storms driven by coronal mass ejections and corotating interaction regions. *Geophys. Res. Lett.* 32, L21105. doi:10.1029/2005GL024590

Miyoshi, Y., Shinohara, I., Takashima, T., Asamura, K., Higashio, N., Mitani, T., et al. (2018a). Geospace exploration project ERG. *Earth Planets Space* 70, 101. doi:10.1186/s40623-018-0862-0

Miyoshi, Y., Shinohara, I., Ukhorskiy, S., Claudepierre, S. G., Mitani, T., Takashima, T., et al. (2022). Collaborative research activities of the Arase and van allen Probes. *Space Sci. Rev.* 218, 38. doi:10.1007/s11214-022-00885-4

Moya, P. S., Pinto, V. A., Sibeck, D. G., Kanekal, S. G., and Baker, D. N. (2017). On the effect of geomagnetic storms on relativistic electrons in the outer radiation belt: Van Allen Probes observations. *JGR. Space Phys.* 122 (11), 2017JA024735. doi:10.1002/2017JA024735

Nasi, A., Daglis, I. A., Katsavrias, C., and Li, W. (2020). Interplay of source/seed electrons and wave-particle interactions in producing relativistic electron PSD enhancements in the outer Van Allen belt. *J. Atmos. Solar-Terrestrial Phys.* 210, 105405. . doi:10.1016/j.jastp.2020.105405

Newell, P. T., and Gjerloev, J. W. (2011). Evaluation of SuperMAG auroral electrojet indices as indicators of substorms and auroral power. *J. Geophys. Res.* 116, A12211. doi:10.1029/2011JA016779

O'Brien, T. P., and Moldwin, M. B. (2003). Empirical plasmapause models from magnetic indices. *Geophys. Res. Lett.* 30, 2002GL016007. doi:10.1029/2002GL016007

Olson, W. P., and Pfitzer, K. A. (1977). *Magnetospheric magnetic field modeling, annual scientific report.* AFOSR Contract No. F44620-75-C-0033

Reeves, G. D., and Daglis, I. A. (2016). "Geospace magnetic storms and the van allen radiation belts," in *Waves, particles and storms in Geospace.* Editors G. Balasis, I. A. Daglis, and I. R. Mann (Oxford, United Kingdom: Oxford University Press).

Reeves, G. D., McAdams, K. L., Friedel, R. H., and O'Brien, T. P. (2003). Acceleration and loss of relativistic electrons during geomagnetic storms. *Geophys. Res. Lett.* 30, 1529. doi:10.1029/2002GL016513

Rodger, C. J., Hendry, A. T., Clilverd, M. A., Forsyth, C., and Morley, S. K. (2022). Examination of radiation belt dynamics during substorm clusters: Activity drivers and dependencies of trapped flux enhancements. *JGR. Space Phys.* 127, e2021JA030003. doi:10.1029/2021JA030003

Sandberg, I., Aminalragia-Giamini, S., Provatas, G., Hands, A., Ryden, K., Heynderickx, D., et al. (2019). Data exploitation of new Galileo environmental monitoring units. *IEEE Trans. Nucl. Sci.* 66 (7), 1761–1769. doi:10.1109/TNS.2019.2915686

Sandberg, I., Jiggens, P., Evans, H., Papadimitriou, C., Aminalragia-Giamini, S., Katsavrias, C., et al. (2021). Harmonization of RBSP and Arase energetic electron measurements utilizing ESA radiation monitor data. *Space weather.* 19, e2020SW002692. doi:10.1029/2020SW002692

Sandberg, I., Provatas, G., Papadimitriou, C., Aminalragia-Giamini, S., Ryden, K., and Evans, H. (2022). *Monitoring Van Allen Radiation Belts using EU Galileo satellites: Observations and Data Products of energetic particle fluxes.* Vienna,

Austria: EGU General Assembly 2022. 23–27 May 2022, EGU22-13001. doi:10.5194/egusphere-egu22-13001

Schiller, Q., Li, X., Blum, L., Tu, W., Turner, D. L., and Blake, J. B. (2014). A nonstorm time enhancement of relativistic electrons in the outer radiation belt. *Geophys. Res. Lett.* 41, 7–12. doi:10.1002/2013GL058485

Schulz, M., and Lanzerotti, L. J. (1974). "Physics and chemistry in space," in *Particle diffusion in the radiation belts* (Bristol, United Kingdom: IOP Publishing), 7. doi:10.1088/0031-9112/26/12/032

Shen, X.-C., Hudson, M. K., Jaynes, A. N., Shi, Q., Tian, A., Claudepierre, S. G., et al. (2017). Statistical study of the storm time radiation belt evolution during van allen Probes era: CME- versus CIR-driven storms. *JGR. Space Phys.* 122 (8), 8327–8339. doi:10.1002/2017ja024100

Shprits, Y. Y., Allison, H. J., Wang, D., Drozdov, A., Szabo-Roberts, M., Zhelavskaya, I., et al. (2022). A new population of ultra-relativistic electrons in the outer radiation zone. *JGR. Space Phys.* 127, e2021JA030214. doi:10.1029/2021JA030214

Shprits, Y. Y., Elkington, S. R., Meredith, N. P., and Subbotin, D. A. (2008). Review of modeling of losses and sources of relativistic electrons in the outer radiation belt I: Radial transport. *J. Atmos. Sol. Terr. Phys.* 70 (14), 1679–1693. doi:10.1016/j.jastp.2008.06.008

Shprits, Y. Y., Meredith, N. P., and Thorne, R. M. (2007). Parameterization of radiation belt electron loss timescales due to interactions with chorus waves. *Geophys. Res. Lett.* 34, L11110. doi:10.1029/2006GL029050

Shue, J.-H., Song, P., Russel, C. T., Steinberg, J. T., Chao, J. K., Zastenker, G., et al. (1998). Magnetopause location under extreme solar wind conditions. *J. Geophys. Res.* 103, 17691–17700. doi:10.1029/98JA01103

Simms, L. E., Engebretson, M. J., Rodger, C. J., Dimitrakoudis, S., Mann, I. R., and Chi, P. J. (2021). The combined influence of lower band chorus and ULF waves on radiation belt electron fluxes at individual L-shells. *JGR. Space Phys.* 126, e2020JA028755. doi:10.1029/2020JA028755

Spence, H. E., Reeves, G. D., Baker, D. N., Blake, J. B., Bolton, M., Bourdarie, S., et al. (2013). Science goals and overview of the radiation belt storm Probes (RBSP) energetic particle, composition, and thermal plasma (ECT) suite on NASA's van allen Probes mission. *Space Sci. Rev.* 179, 311–336. doi:10.1007/s11214-013-0007-5

Staples, F. A., Kellerman, A., Murphy, K. R., Rae, I. J., Sandhu, J. K., and Forsyth, C. (2022). Resolving magnetopause shadowing using multimission measurements of phase space density. *J. Geophys. Res. Space Phys.* 127, e2021JA029298. doi:10.1029/2021JA029298

Thorne, R. M., Li, W., Ni, B., Ma, Q., Bortnik, J., Chen, L., et al. (2013). Rapid local acceleration of relativistic radiation-belt electrons by magnetospheric chorus. *Nature* 504, 411–414. doi:10.1038/nature12889

Tsyganenko, N. A., and Sitnov, M. I. (2005). Modeling the dynamics of the inner magnetosphere during strong geomagnetic storms. *J. Geophys. Res.* 110, A03208. doi:10.1029/2004JA010798

Turner, D. L., Angelopoulos, V., Li, W., Bortnik, J., Ni, B., Ma, Q., et al. (2014). Competing source and loss mechanisms due to wave-particle interactions in Earth's outer radiation belt during the 30 September to 3 October 2012 geomagnetic storm. *JGR. Space Phys.* 119 (3), 1960–1979. doi:10.1002/2014ja019770

Turner, D. L., Angelopoulos, V., Li, W., Hartinger, M. D., Usanova, M., Mann, I. R., et al. (2013). On the storm-time evolution of relativistic electron phase space density in Earth's outer radiation belt. *J. Geophys. Res. Space Phys.* 118, 2196–2212. doi:10.1002/jgra.50151

Turner, D. L., Claudepierre, S. G., Fennell, J. F., O'Brien, T. P., Blake, J. B., Lemon, C., et al. (2015a). Energetic electron injections deep into the inner magnetosphere associated with substorm activity. *Geophys. Res. Lett.* 42, 2079–2087. doi:10.1002/2015GL063225

Turner, D. L., Kilpua, E. K. J., Hietala, H., Claudepierre, S. G., O'Brien, T. P., Fennell, J. F., et al. (2019). The response of Earth's electron radiation belts to geomagnetic storms: Statistics from the Van Allen Probes era including effects from different storm drivers. *JGR. Space Phys.* 124, 1013–1034. doi:10.1029/2018JA026066

Turner, D. L., O'Brien, T. P., Fennell, J. F., Claudepierre, S. G., Blake, J. B., Kilpua, E. K. J., et al. (2015b). The effects of geomagnetic storms on electrons in Earth's radiation belts. *Geophys. Res. Lett.* 42, 9176–9184. doi:10.1002/2015GL064747

Turner, D. L., Shprits, Y., Hartinger, M., and Angelopoulos, V. (2012). Explaining sudden losses of outer radiation belt electrons during geomagnetic storms. *Nat. Phys.* 8 (3), 208–212. doi:10.1038/nphys2185

Usanova, M. E., Drozdov, A., Orlova, K., Mann, I. R., Shprits, Y., Robertson, M. T., et al. (2014). Effect of EMIC waves on relativistic and ultrarelativistic electron populations: Ground based and Van Allen Probes observations. *Geophys. Res. Lett.* 41, 1375–1381. doi:10.1002/2013GL059024

Zhao, H., Baker, D. N., Li, X., Malaspina, D. M., Jaynes, A. N., and Kanekal, S. G. (2019). On the acceleration mechanism of ultrarelativistic electrons in the center of the outer radiation belt: A statistical study. *J. Geophys. Res. Space Phys.* 124, 8590–8599. doi:10.1029/2019JA027111